IOP Publishing New J. Phys. 25 (2023) 113020 https://doi.org/10.1088/1367-2630/ad042e

New Journal of Physics
The open access journal at the forefront of physics

Deutsche Physikalische Gesellschaft DPG
IOP Institute of Physics

Published in partnership with: Deutsche Physikalische Gesellschaft and the Institute of Physics

OPEN ACCESS

RECEIVED
5 April 2023

REVISED
4 August 2023

ACCEPTED FOR PUBLICATION
17 October 2023

PUBLISHED
15 November 2023

PAPER

Capacitive coupling of coherent quantum phase slip qubits to a resonator

Teresa Hönigl-Decrinis[1,2,*], **Ilya Antonov**[3,4], **Rais Shaikhaidarov**[3,4], **Kyung Ho Kim**[3], **Vladimir N Antonov**[3,5] **and Oleg V Astafiev**[3,5]

[1] Institute for Quantum Optics and Quantum Information of the Austrian Academy of Sciences, A-6020 Innsbruck, Austria
[2] Institute for Experimental Physics, University of Innsbruck, A-6020 Innsbruck, Austria
[3] Physics Department, Royal Holloway, University of London, Egham, Surrey TW20 0EX, United Kingdom
[4] National Physical Laboratory, Teddington TW11 0LW, United Kingdom
[5] Skolkovo Institute of Science and Technology, Nobel str. 3, Moscow 143026, Russia
[*] Author to whom any correspondence should be addressed.

E-mail: teresa.hoenigl-decrinis@oeaw.ac.at

Keywords: quantum phase slip, cavity electrodynamics, disordered superconductor, superconducting qubits

Abstract

We demonstrate capacitive coupling of coherent quantum phase slip (CQPS) flux qubits to a resonator patterned on a highly disordered TiN film. We are able to detect and characterise CQPS flux qubits with linewidths down to $\Delta\omega = 12 \pm 1\,\mathrm{MHz}$ on several resonator modes, and show that, unlike inductive coupling, here the coupling strength does not depend on the qubit's energy. Since the qubit is galvanically decoupled from the resonator, our approach provides flexibility in material, design and fabrication choices for CQPS-based devices. Our results are two-fold: we report CQPS in TiN and demonstrate, to our knowledge for the first time, capacitive coupling of a CQPS flux qubit.

1. Introduction

A quantum phase slip is the tunnelling of a quantised flux across a superconducting wire or a weak link, accompanied by a phase jump 2π. The magnetic flux flow generates a dipole voltage $V = \dot{\Phi}$ of amplitude well below the gap of the superconductor (Δ/e). In disordered, quasi-one-dimensional superconducting wires this effect is particularly remarkable demonstrating a coherent quantum phase slip (CQPS), that is exactly dual to coherent Cooper-pair tunnelling in Josephson junctions [1, 2]. Thus complimentary to Josephson junctions, the CQPS centre can be utilised as a non-linear element in superconducting quantum circuits. Direct experiments on the resistance of nanowires did not give conclusive evidence for CQPS, as the Coulomb blockade may not have a quantum and coherent nature [3]. As proposed in [4], placing the narrowing in a superconducting loop with finite inductance allows one to identify the CQPS by their lifting of the degeneracy in the system's energy spectrum, through the coherent exchange of quantised fluxes between the loop and environment. Using radio-frequency measurements CQPS were first experimentally evidenced in such a qubit, where a highly-disordered thin InO_x was used as the CQPS centre [5] and more recently have also been observed in NbN [2, 6, 7]. CQPS have been speculated to exist in other materials such as oxidised granular aluminium AlO_x [8] and TiN [9, 10], the latter of which has been studied in DC measurements. Recently, inverse Shapiro steps, that are quantised current steps from photon-assisted tunnelling of magnetic fluxes through a CQPS centre, have been observed in NbN [11]. The a.c. CQPS is dual to the a.c. Josephson effect, and as such has great significance in the development of future current standards [12].

Here, we demonstrate CQPS in TiN. The superconducting gap of TiN films ($\Delta \sim 180\,\mu\mathrm{eV}$) [2] is smaller compared to that of NbN ($\Delta \sim 1.6\,\mathrm{meV}$) [13] making them more susceptible to thermal noise, but the TiN films are more robust against degradation in time ensuring a more stable lifetime for the devices. This was

evidenced from our experience with NbN films: the normal resistance doubled over a few months. Similar degradation of NbN was noticed in other investigations [14]. Also TiN has one of the largest kinetic inductances because its films are closer to the superconductor-insulator transition [2], allowing for more compact inductive elements. There is also interest of exploring TiN under strong magnetic fields in films of different granularity [9, 15].

We explore TiN CQPS qubits capacitively coupled to a readout resonator, in contrast to earlier experiments that have all used inductive coupling [5–7, 9]. In a scheme with capacitive coupling the resonator is galvanically decoupled from the qubit under investigation, allowing more flexibility in modifying the qubit material independently of the readout circuit—the latter is often most convenient to be made out of aluminium in the same layer as the rest of the auxiliary circuit elements. Differently from inductive coupling, capacitive coupling is predicted to have uniform coupling strength irrespective of the qubit's energy, which is supported by a more uniform visibility of the qubit in a wide field range around the degeneracy point. We perform a full characterisation of the CQPS qubit, reaching a weak-intermediate qubit-resonator coupling regime. Using the master equation formalism we quantify the qubit-resonator avoided crossing.

2. Device details and experimental methods

The CQPS qubits shown in figure 1 comprise of a TiN loop of area S and kinetic inductance L_k interrupted by a narrow wire segment of 50 nm length, and nominal widths ranging from 8 nm to 13.5 nm. The widths were chosen as a balance between realising the 1D transport regime in TiN, with a coherence length $\xi \sim 2$ nm [9], and the attainable resolution of the fabrication process. In the experiment we apply a magnetic field $B_{\rm ext}$ normal to the loop that induces a flux $\Phi_{\rm ext} = B_{\rm ext}S$. In combination with the circulating current, the total flux through the loop is an integer multiple of the magnetic flux quantum $\Phi_0 = h/2e$. To readout the system, we couple the qubit via a capacitance C_{q-r} to a coplanar $\lambda/2$ resonator of TiN. The length and width of the resonator are $L = 1150\,\mu$m and $W = 5\,\mu$m respectively. The impedance of the resonator, $Z_r \sim 3.2\,$kΩ [16], is higher than $Z_0 = 50\,\Omega$ of the transmission line. The strong impedance mismatch gives maximal current at the nodes. Figures 1(c) and (d) shows a micrograph of typical CQPS qubits.

The TiN film is grown with plasma-assisted atomic-layer deposition on a high resistance Si(100) substrate, as described elsewhere [9, 17, 18]. Using d.c. transport measurements, we find its superconducting transition at $T_c \approx 1.2\,$K and normal sheet resistance close to the transition $R_\square \approx 2.63\,$kΩ (see figure 4 in appendix). The transmission line and ground plane are made of normal metal Ti/Au (10 nm/80 nm) on top of the TiN. The rest of the circuit—the phase slip wire, qubit and $\lambda/2$ resonator—are fabricated by dry etching of TiN through a protective mask of 50 nm thick negative resist ma-N 2401 patterned with electron beam lithography—the unprotected TiN thin film undergoes reactive ion etching in a plasma of Ar:CH4 (1:10) to define the required structure. Note that in this work, the CQPS qubit and resonator are patterned in the same lithography layer. However, one can fabricate them in separate steps, which gives the flexibility of using a different material for the resonator. We made a cluster of twelve qubits with different loop sizes, coupled to the same $\lambda/2$ resonator. The chip was mounted in a sample box enclosure in a dilution refrigerator with base temperature of 15 mK. We perform dispersive readout of the qubit states [19] by monitoring the amplitude and phase of the transmitted microwaves while varying the external magnetic flux $\Phi_{\rm ext}$.

The Hamiltonian of a CQPS device in the fluxon basis is

$$H_q = \frac{E_L}{2}\left(\hat{N} - N_{\rm ext}\right)^2 - E_s \cos\left(2\pi\,\hat{n}_q\right), \tag{1}$$

where the circulating current states are expressed in terms of the flux number operator $\hat{N} = \sum N|N\rangle\langle N|$, $N_{\rm ext} = \Phi_{\rm ext}/\Phi_0$ is the normalised induced flux $\Phi_{\rm ext}$; $E_L = \Phi_0^2/L_k$ is the inductive energy; E_s is the flux tunnelling energy. The tunnelling process lifts the energy degeneracy between two flux states $|N\rangle$ and $|N+1\rangle$ (see figure 1(b) [20]). The flux tunnelling operator can be presented as $\cos(2\pi\hat{n}_q) = (|N\rangle\langle N+1| + |N+1\rangle\langle N|)/2$. This describes a two-level system with energy splitting $\hbar\omega_q = \sqrt{(2I_p\delta\Phi)^2 + E_s^2}$ with $\delta\Phi = \Phi - \Phi_0/2$ and $I_p = \Phi_0/2L_k$ the persistent current in the loop.

Let us consider only the two closest states $|N=0\rangle$ and $|N=1\rangle$—the qubit approximation. The Hamiltonian of the qubit-resonator system, with the diagonalised qubit Hamiltonian, resonantly driven through the coupling capacitance C_{r-t} by a classical microwave field of frequency ω and amplitude $V_{\rm in}$ is $H \approx \hbar\omega_q\sigma_z/2 + \hbar\omega_r a^\dagger a + \hbar g(a\sigma^+ + a^\dagger\sigma^-) + \hbar\Omega(a + a^\dagger)\cos(\omega t)$ [21]. The resonator driving amplitude is Ω and the resonator-qubit coupling strength is

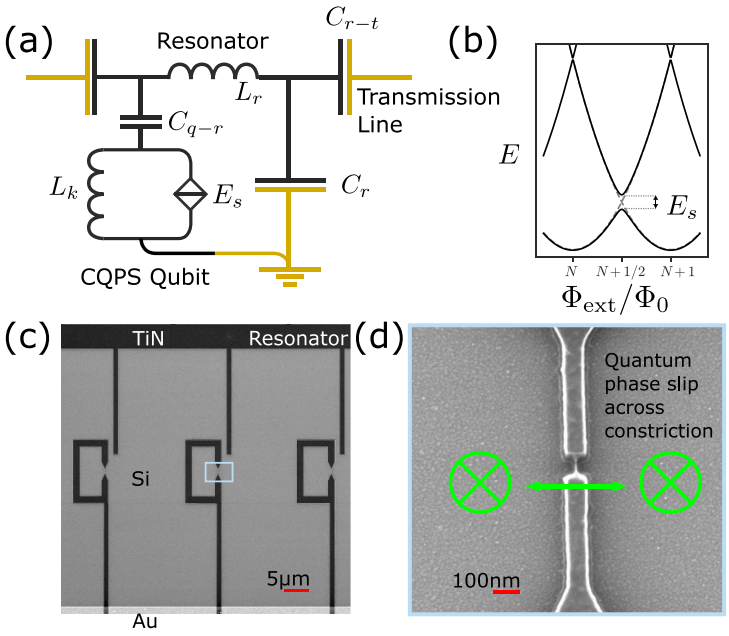

Figure 1. Geometry of CQPS device: (a) Schematic of the $\lambda/2$ resonator capacitively coupled to the transmission line and CQPS qubit with coloured TiN (dark) and Au (yellow); (b) The energy diagram of the qubit at different magnetic flux. The degeneracy is lifted at half flux quantum because of the phase slip energy. (c) The micrograph of the CQPS qubits capacitively coupled via fingers (C_{q-r}) to the TiN resonator. The fingers have a 3 μm overlap with the qubit loop. The CQPS qubit is grounded through the line running to the bottom ground plane; (d) a focused-ion beam micrograph of the constriction in the qubit loop, across which the phase slip occurs (shown in green).

$$\hbar g = \frac{1}{2} V_s C_{q-r} V_m \tag{2}$$

where $V_s = 2\pi E_s/2e$, $V_m = \sqrt{\omega_r/C_r}\cos(m\pi x/L)$ are the zero-point fluctuation amplitudes, C_r is the total resonator capacitance, $m \geqslant 1$ is the resonator mode and x is the position coordinate along the resonator (see appendix B). Here, $a^\dagger$ and a are the photon creation and annihilation operators of the resonator and we define $\sigma_\pm = (\sigma_x \pm i\sigma_y)/2$ where $\sigma_{x,y,z}$ are the Pauli matrices. Compared to inductive coupling (see appendix E), the capacitive coupling strength is uniform away from the degeneracy point, which leads to a better visibility of the qubit across the spectrum. Furthermore, capacitive coupling is natural for a CQPS qubit as the phase-slip process produces voltage.

3. Transmission measurements

First, we characterise the resonator modes with frequencies $f_m = mv/2L$ where $v = 1/\sqrt{L_l C_l}$ is the effective microwave propagation speed for inductance and capacitance per unit length L_l and C_l respectively. Using a vector network analyser we measure the complex microwave transmission t through the system, identifying the dominating resonator modes $m = 2, 3, 4, 5$ with frequencies $f_2 = 3.14$ GHz, $f_3 = 5.12$ GHz, $f_4 = 6.28$ GHz, $f_5 = 7.95$ GHz. The first mode falls outside the measurement range of our equipment 2–12 GHz and is not used. A Lorentzian fit to the peak of $|t|^2$ around f_2 yields the photon decay rate $\kappa/2\pi = 2.78$ MHz corresponding to a loaded quality factor $Q_L = f/(\kappa/2\pi) \approx 1129$. Results for other modes are summarised in table 1.

To characterise the CQPS qubits we perform two-tone spectroscopy measurements. We sweep a probe frequency $f_p = \omega_p/2\pi$ that searches for the qubit at different external field biases B_{ext}, while monitoring the complex transmission t through the readout resonator at f_m. As the coupling strength g varies with the qubit's resonator position x some CQPS qubits are not visible on certain resonator modes. Figure 2(a) shows the two-tone spectroscopy response through the resonator at $f_2 = 3.14$ GHz. In such a dispersive readout, the two states of the qubit are mapped onto two distinct phases of the resonators complex transmission $\arg(t) = \arctan(-(\delta_q \pm g^2/\hbar\omega_q)/\kappa)$ for a detuning of probe signal $\delta_q = 2\pi f_p - \omega_q$ [22]. Around the qubit resonance the phase variation identifies the qubit. The signal has a better contrast for stronger coupling g and

Table 1. Characterised resonator modes.

Resonator mode m	f_m (GHz)	Q_L	$\kappa/2\pi$ (MHz)
2	3.14	1129	2.78
3	5.12	827	6.20
4	6.28	400	15.70
5	7.95	557	14.27

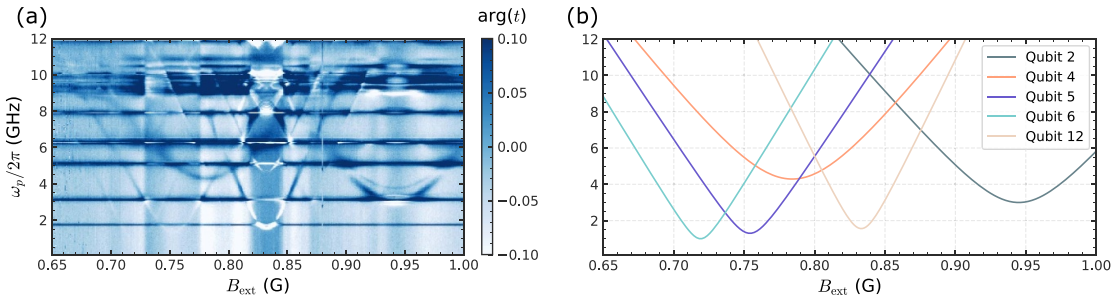

Figure 2. Characterisation of qubits: (a) Two-tone spectroscopy in a narrow range of the external magnetic field. The phase of transmission $\arg(t)$ through the resonator at $f_2 = 3.14$ GHz is monitored while a probe frequency ω_p and external field B_{ext} are independently swept. Strong phase variations occur on qubit resonance $\delta\omega = \omega_p - \omega_q \equiv 0$, which maps out the multiple qubit spectra. The horizontal lines are the resonator modes; (b) line fits to the experimentally measured energy spectrum from the analytical solution of the Hamiltonian (1).

Table 2. Parameters of detected CQPS qubits.

Qubit identifier (width)	E_s (GHz)	E_L (GHz)
1 (8.5 nm)	2.70	26.2
2 (9.0 nm)	3.00	24.0
3 (9.5 nm)	0.98	24.7
4 (10.0 nm)	4.30	21.3
5 (10.5 nm)	1.30	23.9
6 (11.0 nm)	1.00	24.0
9 (13.0 nm)	0.76	20.9
12 (13.5 nm)	1.56	22.2

closer to the degeneracy points. Compared with inductive coupling, the phase contrast will tend to be more uniform as g has a weak energy dependence (refer to appendix E).

By the repetition period, we can identify eight out of the twelve qubits on the sample chip. We extract E_s and E_L from the fit for each identified qubit, see figure 2(b). The results are summarised in table 2 in the main text and table 3 in supplemental A. By normalising the fitted inductances $L = \Phi_0/I_p$ by the number of squares on the perimeters of the CQPS loops, we find $L_\square \approx 7$ nH, and hence a reasonable 63 fF capacitance of the $\lambda/2$ resonator made from the same TiN film. The inductance is larger than the value expected from $L_{k,\square} = \hbar R_\square/\pi\Delta(0) \approx 3.1$ nH. This is an acceptable mismatch for a highly disordered superconductor close to the superconducting insulator transition, in which L_K tends to infinity while resistance remains finite [5].

The phase slip amplitude can be derived from microscopic principles [5, 6, 9] to be of the form $E_s \sim \Delta R_q/R_\xi \exp(-aR_q/R_\xi)$, assuming that there is only a single phase slip centre along the narrow wire segment. Here, R_ξ is the normal state resistance of the wire segment of length ξ, a is on the order of unity [23] and $R_q = h/4e^2$. Using $\Delta = 1.784 T_c k_b$ and $\xi = 2$ nm measured on the same TiN film [9] and constriction widths in the range of $8 - 16$ nm, resulted in E_s that are within the same order of magnitude of those fitted experimentally in table 2—a quantitative agreement cannot be given, since ξ is not defined close to the superconductor-insulator transition [5]. The variation in CQPS amplitudes is unexpectedly low, given that the tunnelling process is exponentially dependent on the sample dimensions and material parameters of the granular structure. There is no apparent dependence on width, indicating that there are multiple phase slip locations along the constriction [7].

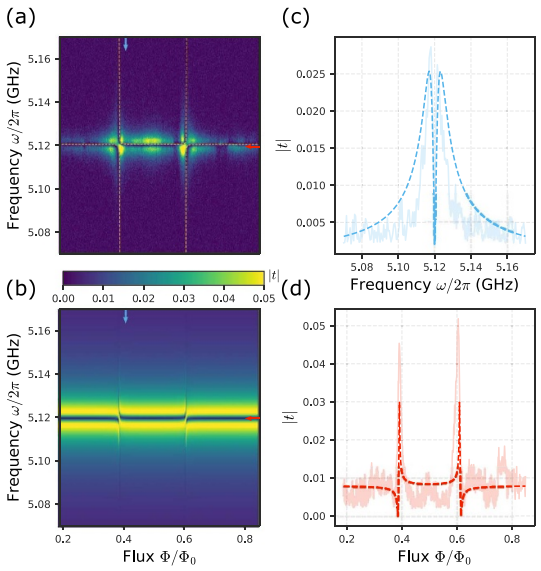

Figure 3. Avoided crossings of qubit 12 on the $m = 3$ resonator mode with cross sections in frequency (blue arrow) and magnetic flux (red arrow): (a) measured transmission spectrum around the $f_3 = 5.12\,\mathrm{GHz}$ resonance. The dashed orange line is the simulated qubit-resonator anticrossing from just the Jaynes–Cummings Hamiltonian; (b) simulated transmission spectrum with using the full master equation formalism of (3); (c), (d) cross section comparing measured and simulated transmission spectra.

4. Modelling the transmission

To model the transmission close to the resonator resonance ($\omega \sim \omega_r$) we use the density matrix ρ and solve the master equation $\dot{\rho} = -i/\hbar[H,\rho] + L[\rho]$ for the stationary case ($\dot{\rho} = 0$). The dissipative Lindblad term $L = L_r + L_q$ presents photon loss in the resonator, $L_r = \kappa(2a\rho a^\dagger - a^\dagger a\rho - \rho a^\dagger a)/2$ (corresponding to jump operator $\sqrt{\kappa}a$ for photon decay), and qubit decoherence, $L_q = \Gamma_1(2\sigma_-\rho\sigma_+ - \sigma_+\sigma_-\rho - \rho\sigma_+\sigma_-)/2 + \Gamma_\phi(\sigma_z\rho\sigma_z - \rho)/2$ where Γ_1, Γ_ϕ are the relaxation and dephasing rate of the qubit respectively (corresponding to energy level fluctuation in qubit $\sqrt{\Gamma_\phi}\sigma_z$ and spontaneous decay $\sqrt{\Gamma_1}\sigma^-$). In the weak driving limit, when the mean photon number in the resonator is less than one, the photon space can be truncated to two levels $\{|n=0\rangle, |n=1\rangle\}$ and $\mathcal{O}(\Omega^2) \to 0$ (see appendix D for a justification based on multi-photon spectrum measurements). In this regime, the transmission coefficient has an analytical expression (see appendix C)

$$t = \frac{V_{\mathrm{out}}}{V_{\mathrm{in}}} = -i\frac{1}{2}\frac{C_{r-t}^2\omega^2 Z}{C_r}\left[\frac{1}{g^2/\delta_q' - \delta_r'} + \mathrm{h.c.}\right], \tag{3}$$

where h.c. represents the Hermitian conjugate, $\delta_q' = \delta_q + i(\Gamma_1/2 + \Gamma_\phi)$, $\delta_r' = \delta_r + i\kappa/2$, $Z = 50\,\Omega$ transmission line impedance, $C_r = 63\,\mathrm{fF}$ is evaluated from the measured sheet inductance and resonator geometry, $C_{r-t} = \sqrt{\kappa C_r/2Z}/\omega_r \sim 2\,\mathrm{fF}$ [24], and $\omega = 2\pi f$ is the single tone applied to the system.

We measure the complex transmission t in a narrow range centred around the resonator modes f_m for one of the qubits, which will be dominated by the strong resonator response. By subtracting the average transmission value at each frequency, we separate out the avoided crossings due to the finite coupling g predicted by (3), which we demonstrate in figure 3 for qubit 12 on resonator mode $m = 3$. We fit each individual avoided crossing to extract the coupling g and arrive at $g = 24.4, 18, 27.1$ and $33.8\,\mathrm{MHz}$ for modes $2, 3, 4$ and 5 respectively, summarised in table 4 and achieve reasonable agreement with (2).

Equation (3) nicely captures the features of the avoided crossings using $\kappa/2\pi = 6.2\,\mathrm{MHz}$ (see table 1) and $\Gamma_2/2\pi \sim 3.6 \pm 0.4\,\mathrm{MHz}$ found from qubit characterisation at its degeneracy point (see figure 5 in appendix), and the signal attenuation and amplification in the inputs and output lines. The vanishing of the transmission peak at qubit-resonator resonance point $\sim 0.39\,\Phi_0$ indicates the weak-intermediate coupling regime [24] where $g > \kappa, \Gamma_1$. Overall we achieved good characterisation of a CQPS qubit read out using a capacitively coupled resonator. The coupling strength is independent of the position in the flux period, with different strengths on the different modes and allows for further investigation of CQPS devices using a different material.

In conclusion, we have fabricated and measured capacitively coupled TiN CQPS qubits. TiN is a new material currently under study for application with the CQPS devices. We experimentally observed and theoretically analysed operation of the eight TiN CQPS qubits, which demonstrate linewidths as low as $\Delta\omega = 12 \pm 1$ MHz. The CQPS qubits are galvanically decoupled from the resonator, providing flexibility in the choice of material for the circuit. Thus one can use non-superconducting materials for the ground plane, transmission line and resonator, and study of CQPS-based qubits in high magnetic field environments, where properties of high-inductance film can be modified.

Data availability statement

The data that support the findings of this study will be openly available following an embargo at the following URL/DOI: https://github.com/creamy-seas/coherent-quantum-phase-slip-data.

Acknowledgments

We thank T M Klapwijk for providing the TiN films and S de Graaf for fruitful comments on the manuscript. Samples were fabricated at SuperFab of Royal Holloway, University of London. This project was supported by European Union's Horizon 2020 Research and Innovation Programme under Grant Agreement No. 862660/QUANTUM E-LEAPS and EMPIR 20FUN07 SuperQuant, and UK Engineering and Physical Sciences Research Council (EPSRC) Grant No. EP/T004088/1. T H-D acknowledges financial support from the Lise Meitner programme of the Austrian Science Fund (FWF), Project No. M3347.

Appendix A. Auxiliary tables and figures

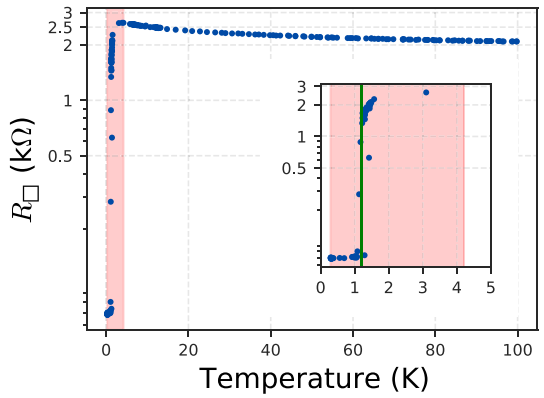

Figure 4. Sheet resistance measured of TiN monitored during cooldown on a 80 × 20 μm TiN 95 cycle bar. An estimate of the kinetic inductance $L_\square = \hbar R_\square/\pi\Delta(0) \approx 3.1\,\mathrm{nH}$ can be made using the superconducting transition temperature $T_c = 1.2\,\mathrm{K}$ (green line). The inset gives a close up view of the transition point (red region).

Table 3. Extended table of parameters of detected CQPS qubits.

Qubit id	x/L	E_s (GHz)	E_L (GHz)	Period (mA)
1	0.550	2.70	26.2	0.42 750
2	0.530	3.00	24.0	0.34 870
3	0.510	0.98	24.7	0.33 000
4	0.511	4.30	21.3	0.28 170
5	0.531	1.30	23.9	0.26 850
6	0.551	1.00	24.0	0.25 550
9	0.500	0.78	20.9	0.20 694
12	0.561	1.56	22.2	0.18 180

Appendix B. Capacitive coupling

The necessary condition for the derivation below is $C_{q-r} \gg C_S$ where C_S is the kinetic capacitance of the CQPS junction. To achieve coupling between the resonator-qubit system, the qubit is placed in the middle of a $\lambda/2$ resonator (at a current antinode, voltage node), where the magnetic field of the resonator has a maximum. The coplanar resonator voltage field operator can be expressed as

$$\hat{V}_r = V_m i\left(a - a^\dagger\right), \tag{B1}$$

where $V_m = \sqrt{\hbar\omega_m/C_r}\cos(m\pi x/L)$ is the voltage of the mth resonator mode at position x in the resonator and C_r is the total resonator capacitance. The coupling Hamiltonian of the resonator-qubit system is given by

$$H_{\mathrm{int}} = \hat{V}_q C_{q-r} \hat{V}_r, \tag{B2}$$

where C_{q-r} is the coupling capacitance, $\hat{V}_q$ and $\hat{V}_r$ are the qubit and resonator voltage operators respectively. To derive the qubit voltage operator $\hat{V}_q$ we rewrite the qubit Hamiltonian of (1) in the form

$$H_q = \frac{E_L}{2}\left(\hat{N} - N_{\mathrm{ext}}\right)^2 - E_s \cos\left[2\pi\left(\hat{n}_q + \delta n_q\right)\right], \tag{B3}$$

where δn_q is an induced charge along the CQPS junction (e.g. a wire). The qubit voltage operator couples the adjacent fluxon states $|N\rangle$ and $|N+1\rangle$ [1] and is defined by

$$\hat{V}_q = \frac{1}{2e}\frac{\partial H_q}{\partial \delta n_q} = \frac{2\pi E_s}{2e}\sin\left[2\pi\left(\hat{n}_q + \delta n_q\right)\right]. \tag{B4}$$

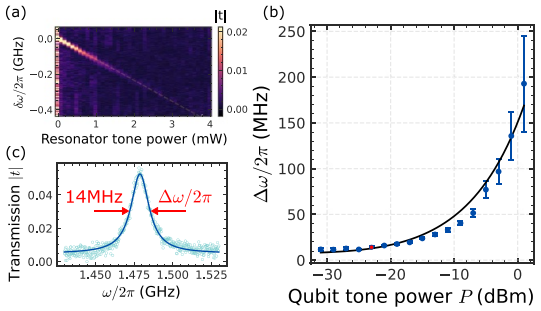

Figure 5. Qubit 12 characterisation through its: (a) AC Stark shift measuring the change of the qubit's transition frequency ($\delta\omega$) in response to a power sweep of the resonator tone at the degeneracy point ∼1.5 GHz (see figure 2). The linear response indicates the presence of a coupled qubit on the resonator and can be used to calibrate the photon number in the resonance mode; **(b)** Spectral linewidth $\Delta\omega = 2\sqrt{\Gamma_2^2 + \alpha \times P}$ which extracts a decoherence rate $\Gamma_2 = 3.6 \pm 0.4$ MHz [25]. The linewidths are measured using two-tone spectroscopy described in figure 2 and fitted with Lorentzian ($\propto 1/1 + (2(\omega - \omega_0)/(\Delta\omega))^2$ as shown in **(c)** for the red data point. The linewidth of this TiN CQPS qubit goes down to 12 ± 1 MHz at the lowest powers, narrower than than for previous qubits made from NbN (26 MHz [7]) and InO_x (260 MHz [5]).

Note that in our qubit, with the CQPS junction shunted by an inductor, the DC charge offset δn_q is zero. We introduce the phase-slip voltage $V_s = 2\pi E_s/2e$ [1, 9] and then, using the expression $\exp(2\pi\hat{n}_q) = \sum |N+1\rangle\langle N|$, rewrite the qubit voltage operator in the matrix form

$$\hat{V}_q = \frac{V_s}{2}\sum_N \left(-i|N+1\rangle\langle N| + i|N\rangle\langle N+1|\right). \tag{B5}$$

The phase slip voltage operator couples two neighbouring fluxoid states $|N\rangle$, $|N+1\rangle$ and can be simplified for the truncated space $\{|N=0\rangle, |N=1\rangle\}$ in the form

$$\hat{V}_q \approx -\frac{V_s}{2}\sigma_y. \tag{B6}$$

Inserting equations (B1) and (B5) into equation (B2) we find the interaction qubit-resonator term

$$H_{\text{int}} = \hbar g i \left(a - a^\dagger\right)\sigma_y, \tag{B7}$$

where the qubit-resonator coupling strength g is defined

$$\hbar g = \frac{1}{2} V_s C_{q-r} V_m. \tag{B8}$$

Note that the interaction term does not change in the transformation from the physical basis $\{|N=0\rangle, |N=1\rangle\}$ (fluxon states) to the energy eigenbasis $\{|g\rangle, |e\rangle\}$, as the unitary transformation diagonalising the qubit Hamiltonian (1) ($U_y(\theta/2) = \exp[-i\sigma_y\theta/2]$, $\tan(\theta) = E_s/2I_p\delta\Phi$) commutes with (B7). Omitting $a^\dagger\sigma^+$ and $a\sigma^-$ terms we obtain the standard Jaynes–Cummings interaction term $H_{\text{int}} = \hbar g(a\sigma^+ + a^\dagger\sigma^-)$.

To summarise, the different terms of the expression for g can be understood as follows: $V_s = 2\pi E_s/2e$ is the voltage on the CQPS qubit associated with a phase slip event, C_{q-r} is the capacitance coupling the resonator-qubit system, $V_m = \sqrt{\hbar m\omega/C_r}\cos(m\pi x/L)$ is the voltage of the mth resonator mode, and the cosine term comes from the position dependence (x) of the standing waves in the resonator.

Table 4 demonstrates the fitted $g/2\pi$ parameters for qubits on the different resonator modes, taking the E_s from the spectrum fittings in table 2. The fitted coupling strengths expected are in general agreement to those predicted by (B8), with weaker coupling resulting in a larger disparity.

Table 4. Summary of fits to various qubit-resonator anticrossings. Expected values are evaluated with (2), using the qubits energies in table 2, resonator parameters in table 1 and a coupling capacitor $C_{q-r} = 0.3$ fF that reproduces the experimental values well.

Qubit	Mode m	$g/2\pi$ expected (MHz)	$g/2\pi$ fitted (MHz)
3	2	16.5	16.4
	3	2.5	2.6
	4	23.1	23.0
5	2	21.6	21.5
	3	8.0	7.8
6	2	16.0	16.0
	3	10.1	9.8
12	2	24.5	24.4
	3	18.3	18.0
	4	27.0	27.1
	5	34.3	33.8

Appendix C. Transmission profile

The master equation:

$$\begin{aligned}\dot{\rho} &= -\frac{i}{\hbar}\left[\mathcal{H},\rho\right] + \mathcal{L}\left[\rho\right] \\ &= -i\frac{\delta_q}{2}\left[\sigma_z\rho - \rho\sigma_z\right] - i\delta_r\left[a^\dagger a\rho - \rho a^\dagger a\right] \\ &\quad - ig\left[a\sigma_+\rho - \rho a\sigma_+ + a^\dagger\sigma_-\rho - \rho a^\dagger\sigma_-\right] \\ &\quad - i\frac{\Omega}{2}\left[a\rho - \rho a + a^\dagger\rho - \rho a^\dagger\right] + \frac{\kappa}{2}\left[2a\rho a^\dagger - a^\dagger a\rho - \rho a^\dagger a\right] \\ &\quad + \frac{\Gamma_1}{2}\left[2\sigma_-\rho\sigma_+ - \sigma_+\sigma_-\rho - \rho\sigma_+\sigma_-\right] + \frac{\Gamma_\phi}{2}\left[\sigma_z\rho\sigma_z - \rho\right]\end{aligned} \tag{C1}$$

is solved in the qubit-resonator basis $|e,n\rangle, |e,n+1\rangle, |g,n\rangle, |g,n+1\rangle$ in the case of low photon number in the resonator ($n=0$ and $n=1$).

An analytical solution is found by evaluating for the stationary state $\dot{\rho}=0$ and using the low drive limit where $\mathcal{O}(\Omega^2)\to 0$. Such evaluation directly gives the expectation value

$$\begin{aligned}\left\langle a^\dagger\right\rangle &= \mathrm{Tr}\left\{a\rho\right\} = \rho_{10} + \rho_{32} \\ &= \frac{\Omega/2}{\frac{g^2}{\delta_q + i\left(\frac{\Gamma_1}{2}+\Gamma_\phi\right)} - \left(\delta_r + i\frac{\kappa}{2}\right)}.\end{aligned} \tag{C2}$$

The expectation value (C2) defines the field in the resonator (rotated relative to equation (B1) by a phase factor):

$$V_r\left(\left\langle a\right\rangle + \left\langle a^\dagger\right\rangle\right). \tag{C3}$$

This field induces a displacement current across capacitance C_k through which the resonator couples to the output line ($I_d = V_r/Z_{\mathrm{gap}} = V_r/(1/i\omega C_k)$) which generates a voltage in the output transmission line with impedance Z

$$V_{\mathrm{out}}\left(t\right) \approx V_r\left(\left\langle a\right\rangle + \left\langle a^\dagger\right\rangle\right)\left[i\omega C_k\right]Z \tag{C4}$$

Substituting in the values will give

$$\begin{aligned} V_{\text{out}}(t) &= -i\omega C_k Z V_r \left[\frac{\Omega/2}{g^2/\delta_q' - \delta_r'} + \text{h.c.}\right] \\ &= -i\omega C_k Z V_r \frac{\Omega}{2}\left[\frac{1}{g^2/\delta_q' - \delta_r'} + \text{h.c.}\right] \\ &= -i\omega C_k Z V_r \left[\frac{C_k V_{\text{in}} V_r}{\hbar}\frac{1}{2}\right]\left[\frac{1}{g^2/\delta_q' - \delta_r'} + \text{h.c.}\right] \\ &= -i\omega C_k^2 Z V_{\text{in}} \left[\frac{1}{\hbar}\frac{1}{2}\right]\frac{\hbar\omega}{C_r}\left[\frac{1}{g^2/\delta_q' - \delta_r'} + \text{h.c.}\right] \\ &= -i\frac{1}{2}V_{\text{in}}\frac{C_k^2\omega^2 Z}{C_r}\left[\frac{1}{g^2/\delta_q' - \delta_r'} + \text{h.c.}\right] \end{aligned} \tag{C5}$$

where: $\delta_q' = \delta_q + i(\Gamma_1 2 + \Gamma_\phi)$ and $\delta_r' = \delta_r + i\kappa/2$ and h.c. is the Hermitian conjugate. Then a simple ratio gives the transmission coefficient:

$$t = \frac{V_{\text{out}}}{V_{\text{in}}} = -i\frac{1}{2}\frac{C_k^2\omega^2 Z}{C_r}\left[\frac{1}{g^2/\delta_q' - \delta_r'} + \text{h.c.}\right]. \tag{C6}$$

Appendix D. Justification for weak driving regime

Multiple photon excitations are visible when the system is subject to a strong drive of −10 dBm, see figure 6. Each of the simulated lines corresponds to $\pm\omega_{\text{qubit}} \pm n\omega_{\text{resonator}}$ for $n = 0, 1, 2, 3$. Multi-photon processes with $n > 4$ are not resolvable. For the qubit characterisation measurements, in figure 2 and figure 3, the driving power was −25 dBm (30 times weaker), eliminating $n > 1$ processes and allowing for both $|n = 0\rangle, |n = 1\rangle$ and $\mathcal{O}(\Omega^2) \to 0$ approximations to be made in the solution of the master equation (3).

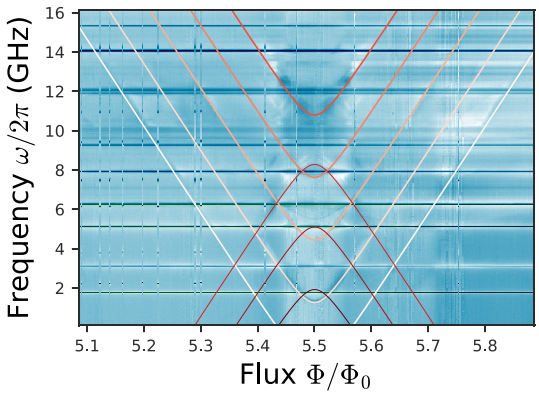

Figure 6. Multi-photon processes under strong drive: Spectrum of a qubit is taken under a strong −10 dBm drive at room temperature (subsequent attenuation of −83 dB inside the cryostat was the same for all measurements) showing the $\pm n = 3$ photon excitation processes.

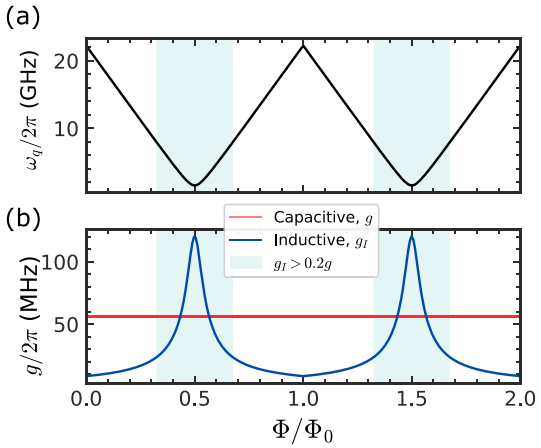

Figure 7. Comparison of inductive and capacitive coupling strengths: (a) Energy of a CQPS qubit as a function of the magnetic field evaluated with (1); (b) Comparison of inductive (blue, g_I) and capacitive (red, g) coupling strengths at different values of $\omega_q(\Phi)$. Inductive coupling strength peaks at the flux degeneracy points, getting substantially weaker away from it (region where qubit has good inductive coupling $g_I > 0.2g$ is shaded in blue). Experimentally this weak interaction makes it harder to detect the CQPS qubit away from the degeneracy point. Simulations were run for a resonator $C_r = 60\,\mathrm{fF}, L_r = 1600\,\mathrm{nH}, E_s/h = 1.5\,\mathrm{GHz}$ and $M = 10\,\mathrm{nH}$ (12 pH used in [5]).

Appendix E. Inductive coupling

Galvanic coupling of the qubit's persistent current I_p and the resonator current I_r via a shared inductance M is represented in the persistent current basis by [5, 26]

$$H_{\mathrm{int}} = \hat{I}_r M I_p \sigma_z. \tag{E1}$$

Diagonalising the Hamiltonian using the same $U_y(\theta/2)$ rotation as appendix B transforms this interaction term into a representation in the qubit eignebasis $\{|g\rangle, |e\rangle\}$

$$\begin{aligned} H'_{\mathrm{int}} &= \hat{I}_r M I_p U_y^{\dagger}(\theta/2)\,\sigma_z U_y(\theta/2) \\ &= \hat{I}_r M I_p \left(\cos(\theta)\,\sigma_z + \sin(\theta)\,\sigma_x\right) \\ &= \hat{I}_r M I_p \left(\frac{2I_p\delta\Phi}{\hbar\omega_q}\sigma_z + \frac{E_s}{\hbar\omega_q}\sigma_x\right). \end{aligned} \tag{E2}$$

Inserting the resonator current [27] for the odd modes at $x = 0$ (even modes $\propto \sin(k_m x)$ have a node at $x = 0$ and thus do not contribute) $\hat{I}_r = I_m(a + a^{\dagger})\cos(k_m x), I_m = \sqrt{\hbar m\omega_r/2L_r}$

$$\begin{aligned} H'_{\mathrm{int}} &= I_m M I_p \left(a + a^{\dagger}\right)\left(\frac{2I_p\delta\Phi}{\hbar\omega_q}\sigma_z + \frac{E_s}{\hbar\omega_q}\sigma_x\right) \\ &= \hbar g_I \left(a + a^{\dagger}\right)\left(\frac{2I_p\delta\Phi}{E_s}\sigma_z + \sigma_x\right), \end{aligned} \tag{E3}$$

with a coupling strength

$$\hbar g_I = I_m M I_p \frac{E_s}{\hbar\omega_q}. \tag{E4}$$

Finally, transforming (E3) into a form that resembles the Jaynes–Cumming Hamiltonian by moving into the interaction picture using rotation $U = \exp[iH_q t/\hbar]$

$$\begin{aligned} UH'_{\mathrm{int}}U^{\dagger} = {} & \hbar g_I \left(a\sigma_+ e^{i\left(\omega_q-\omega_r\right)t} + \mathrm{h.c.}\right) \\ & \times \hbar g_I \left(a\sigma_- e^{-i\left(\omega_q+\omega_r\right)t} + a^{\dagger}\sigma_+ e^{+i\left(\omega_q+\omega_r\right)t} + \mathrm{h.c.}\right) \\ & \times \hbar g_I \frac{2I_p\delta\Phi}{E_s}\sigma_z \left(a e^{-i\omega_r t} + a^{\dagger} e^{i\omega_r t}\right). \end{aligned} \tag{E5}$$

The last term in (E5) will be a modification to the qubit energy, while the middle term is ignored in the rotating wave approximation when $\omega_q \sim \omega_r$, leaving

$$\hbar g_I \left(a\sigma_+ + a^\dagger \sigma_-\right) \tag{E6}$$

as the term describing inductive interaction between the qubit and resonator in analogy to (B7).

As seen from (E4), the coupling strength depends on the energy ($\hbar\omega_q$), or effectively the bias magnetic field ($\delta\Phi$), which is not present in capacitive coupling (see (B8)). This is because capacitive coupling is traverse ($g \propto \sigma_y$) which promotes a direct flux state exchange, while inductive coupling is longitudinal ($g \propto \sigma_z$) which instead modifies the persistent current of and hence the energy of the qubit. Figure 7 illustrates the difference in behaviour of the coupling strengths as a function of flux.

ORCID iDs

Teresa Hönigl-Decrinis https://orcid.org/0000-0003-3450-0874
Ilya Antonov https://orcid.org/0000-0002-8809-953X
Vladimir N Antonov https://orcid.org/0000-0002-0415-5267
Oleg V Astafiev https://orcid.org/0000-0001-5763-589X

References

[1] Mooij J E and Nazarov Y V 2006 *Nat. Phys.* **2** 169–72
[2] de Graaf S E *et al* 2018 *Nat. Phys.* **14** 590–4
[3] Arutyunov K, Golubev D and Zaikin A 2008 *Phys. Rep.* **464** 1
[4] Mooij J E and Harmans C J P M 2005 *New J. Phys.* **7** 219
[5] Astafiev O V, Ioffe L B, Kafanov S, Pashkin Y A, Arutyunov K Y, Shahar D, Cohen O and Tsai J S 2012 *Nature* **484** 355–8
[6] Peltonen J T *et al* 2013 *Phys. Rev.* B **88** 220506
[7] Peltonen J T, Peng Z H, Korneeva Y P, Voronov B M, Korneev A A, Semenov A V, Gol'tsman G N, Tsai J S and Astafiev O V 2016 *Phys. Rev.* B **94** 180508
[8] Schön Y, Voss J N, Wildermuth M, Schneider A, Skacel S T, Weides M P, Cole J H, Rotzinger H and Ustinov A V 2020 *npj Quantum Mater.* **5** 1
[9] de Graaf S E, Shaikhaidarov R, Lindström T, Tzalenchuk A Y and Astafiev O V 2019 *Phys. Rev.* B **99** 205115
[10] Schneider I, Kronfeldner K, Baturina T I and Strunk C 2019 *Phys. Rev.* B **99** 094522
[11] Shaikhaidarov R S, Kim K H, Dunstan J W, Antonov I V, Linzen S, Ziegler M, Golubev D S, Antonov V N, Il'ichev E V and Astafiev O V 2022 *Nature* **608** 45
[12] Wang Z M, Lehtinen J S and Arutyunov K Y 2019 *Appl. Phys. Lett.* **114** 242601
[13] Bell M, Sergeev A, Mitin V, Bird J, Verevkin A and Gol'tsman G 2007 *Phys. Rev.* B **76** 094521
[14] Amin K R, Ladner C, Jourdan G, Hentz S, Roch N and Renard J 2022 *Appl. Phys. Lett.* **120** 164001
[15] Schneider I, Kronfeldner K, Baturina T I and Strunk C 2019 *Phys. Rev. B* **99** 094522
[16] $Z = \sqrt{1/(vC_l)^2}$—using a calibrated capacitance per unit length $C_l \sim 0.85 \times 10^{-10}$ F/m and wave velocity $v = 2Lf_1 = Lf_2$ determined from the measured resonance $f_2 = 3.14$ GHz
[17] Coumou P C J J, Driessen E F C, Bueno J, Chapelier C and Klapwijk T M 2013 *Phys. Rev.* B **88** 180505
[18] Linzen S, Ziegler M, Astafiev O V, Schmelz M, Hübner U, Diegel M, Il'ichev E and Meyer H-G 2017 *Supercond. Sci. Technol.* **30** 035010
[19] Blais A, Huang R-S, Wallraff A, Girvin S M and Schoelkopf R J 2004 *Phys. Rev.* A **69** 062320
[20] Mooij J E and Harmans C J P M 2005 *New J. Phys.* **7** 219
[21] Walls D F and Milburn G J 2008 *Quantum Optics* (Springer)
[22] Gambetta J, Blais A, Schuster D I, Wallraff A, Frunzio L, Majer J, Devoret M H, Girvin S M and Schoelkopf R J 2006 *Phys. Rev.* A **74** 042318
[23] Vanević M and Nazarov Y V 2012 *Phys. Rev. Lett.* **108** 187002
[24] Oelsner G *et al* 2010 *Phys. Rev.* B **81** 172505
[25] Bolgar A N, Zotova J I, Kirichenko D D, Besedin I S, Semenov A V, Shaikhaidarov R S and Astafiev O V 2018 *Phys. Rev. Lett.* **120** 223603
[26] Skacel S T 2018 *PhD Thesis* Karlsruher Institut für Technologie (KIT)
[27] Lindström T, Webster C H, Healey J E, Colclough M S, Muirhead C M and Tzalenchuk A Y 2007 *Supercond. Sci. Technol.* **20** 814